THE ASTROPHYSICAL JOURNAL, 410:764–776, 1993 June 20

THE BOW SHOCK AND MACH DISK OF HH 111V

JON A. MORSE[1,2]
Department of Physics and Astronomy, University of North Carolina, CB 3255, Phillips Hall, Chapel Hill, NC 27599-3255
STEVE HEATHCOTE
Cerro Tololo Inter-American Observatory, Casilla 603, La Serena, Chile
GERALD CECIL
Department of Physics and Astronomy, University of North Carolina, CB 3255, Phillips Hall, Chapel Hill, NC 27599-3255
PATRICK HARTIGAN
Five College Astronomy Department, Graduate Research, Tower B, 517G, University of Massachusetts, Amherst, MA 01003
AND
JOHN C. RAYMOND
Harvard-Smithsonian Center for Astrophysics, 60 Garden Street, Cambridge, MA 02138
Received 1992 October 16; accepted 1992 December 23

ABSTRACT

We present spatially resolved line profiles in Hα and [S II] λλ6716, 6731 across the working surface region in the Herbig-Haro object HH 111V. Data were acquired with the Rutgers/CTIO imaging Fabry-Perot interferometer on the CTIO 4 m telescope at ~1".3 FWHM spatial and ~35 km s^{-1} FWHM kinetic resolution. We separate Mach disk emission spatially and kinematically from the bow shock emission. We have used the Hα flux measured at the apex of the bow shock to estimate the preshock density of ~200 cm^{-3}. Our detailed measurements of the electron density as a function of position and velocity across the bow shock, combined with new models of the bow shock emission, show that an ambient magnetic field of ~30 μG inhibits the compression of the postshock gas. Our models indicate that the magnetic field also contributes to extending the cooling distance behind the shock to resolvable scales, as observed in the spatial separation of [S II] and Hα in the emission-line images of Reipurth et al. However, the ram pressure at the bow shock HH 111V exceeds the magnetic energy density by a factor of ~10^3, so the magnetic field is not large enough to change the direction of the flow.

The preshock medium must flow away from the stellar energy source at ~300 km s^{-1} to account for the observed kinematics of the line emission in HH 111V. Hence, this working surface is a secondary ejection moving into the wake of an earlier ejection. HH 111 is the third case (HH 34 and HH 47 are other examples) of a stellar jet where the brightest bow shock moves into the wake of a previous high-velocity ejection. Balancing the ram pressures in the bow shock and Mach disk yields an estimated jet-to-ambient density ratio ~10, similar to our previous estimate for the HH 34 jet (Morse et al.).

Subject headings: shock waves — stars: individual (HH 111) — stars: pre–main-sequence

1. INTRODUCTION

There is strong evidence that stellar jets are driven by circumstellar accretion disks associated with T Tauri–like stars (see Königl & Ruden 1992 for a review). Although large amounts of angular momentum must transfer from the disk to the star during accretion, most T Tauri stars rotate at only a small fraction of their breakup velocities (e.g., Vogel & Kuhi 1981; Hartmann et al. 1986). Vigorous mass loss in the form of high-velocity, bi-polar collimated outflows is the most likely mechanism by which pre–main-sequence stars dissipate the angular momentum gained during the accretion of surrounding material. Investigating the dynamics of stellar jets probes the time history of the outflow and, therefore, of the disk accretion. Recent observations of multiple bow shocks along several stellar jets (e.g., HH 46/47, see Hartigan, Raymond, & Meaburn 1990; Reipurth & Heathcote 1991; HH 34, see Reipurth & Heathcote 1992) suggest that outflows from young stars are non-steady, and may be related to FU Ori–type outbursts.

Ground-based observations can be used to study stellar jets in detail because the shocks are spatially resolved and produce optical line emission. Radial velocities and proper motions of the line emission describe the kinematic structure of stellar jets, and emission-line ratios constrain the shock velocities, ionization states, and densities. These data also provide insight into the dynamical structure of jets and their interaction with the surrounding environment. Observational constraints on jet physics are useful because stellar jets are difficult to model in detail.

The bow shock/Mach disk morphology is a common feature in numerical stimulations of the heads of radiative stellar jets (e.g., Raga 1988; Blondin, Königl, & Fryxell 1989; Stone & Norman 1993; Gouveia Dal Pino & Benz 1993). The bow shock excites and accelerates ambient gas while the Mach disk decelerates jet material impinging on the ambient medium; the two shocks together comprise the "working surface" (Blandford & Rees 1974). Recent observations (e.g., Reipurth & Heathcote 1991) have shown that it is possible to distinguish

[1] Visiting Astronomer, Cerro Tololo Inter-American Observatory, operated by the National Optical Astronomy Observatories under contract to the National Science Foundation.
[2] Present address: Space Telescope Science Institute, 3700 San Martin Drive, Baltimore, MD 21218.

the Mach disk emission from the post–bow shock emission in Herbig-Haro stellar jet systems, as predicted by Hartigan (1989). We have presented Fabry-Perot observations and shock models of the HH 34 working surface (Morse et al. 1992, hereafter Paper I) which enabled us to separate the Mach disk emission spatially and kinematically from the bow shock emission. The large [S II]/Hα line ratios and low electron densities in the HH 34 Mach disk show that the shock velocity there is low. In this paper we present similar observations and shock models of the prominent working surface labeled HH 111V by Reipurth (1989a).

The HH 111 stellar jet was discovered by Reipurth (1989a) in the region of the Orion B molecular cloud complex. HH 111 is an optical bipolar outflow with a bright, highly collimated jet evident in the approaching lobe that terminates at the working surface HH 111V ~ 140″ away from an embedded class I *IRAS* point source, which probably powers the entire complex (Reipurth & Olberg 1991). The morphological similarities between the HH 111 and HH 34 outflows have been discussed by Reipurth (1989b). Unlike HH 34, Reipurth & Olberg found a major molecular outflow associated with HH 111. Reipurth (1989a) presented long-slit spectra of the visible jet and bow shock V showing low-excitation emission indicative of radiative shock waves.

Reipurth, Raga, & Heathcote (1992, hereafter RRH) measured proper motions in the HH 111 system and combined these results with radial velocities reported in Reipurth (1989a) to find the angle of inclination. Assuming a distance to HH 111 of 460 pc, the tangential velocity measured in the bow shock V was ~392 km s^{-1}, with an estimated uncertainty of ~20%. The heliocentric radial velocity peaks at ~ −56 km s^{-1} and must be added to the systemic velocity of the embedded driving source at +23 km s^{-1}, to yield an angle of inclination to the line of sight $\phi \sim 80°$, implying a space velocity of ~400 km s^{-1} for the working surface region HH 111V. RRH also discussed the structure and excitation of the approaching bow shock HH 111V and reported a [S II] bright region in the working surface just behind the apex of the bow shock which they identified as the Mach disk.

We discuss our Fabry-Perot observations and reductions in § 2 and present the grids of spectral line profiles and maps of the electron densities [S II]/Hα ratios in § 3. In § 4 we discuss our model of the bow shock, constructed from new planar shock models that are optimized for this system. We assess the importance of the ambient magnetic field by comparing our data in detail with this bow shock model. We also discuss our identification of the Mach disk associated with HH 111V, which differs from that made by RRH. Our results are summarized in § 5.

2. FABRY-PEROT OBSERVATIONS AND REDUCTIONS

The Rutgers/CTIO CCD-based imaging Fabry-Perot was used on the CTIO 4 m telescope in 1992 January in ~1.″3 FWHM seeing to obtain full spatial and partial kinematic sampling of the HH 111 system in the Hα and [S II] λλ6716, 6731 emission lines. The detector was the TEK4 CCD which provided an image scale of ~0.″4 pixel^{-1} and field of diameter ~2.′5. The "narrow" etalon was used which had a free spectral range of 18 Å and FWHM resolution of 0.7 Å. Narrow-band filters were placed in the collimated beam in front of the etalon in order to pass ~1 spectral order. The central wavelengths (FWHM bandpasses) for the Hα and [S II] filters were 6563 Å (17 Å), 6718 Å (22 Å), and 6732 Å (22 Å), respectively. The exposure times were 900 for the [S II] images and 600 s for the Hα images. The Hα data were scaled to reflect the different exposure times when obtaining image ratios. The images were bias-subtracted and corrected for atmospheric extinction using standard IRAF routines.

Our Fabry-Perot imaging and reduction techniques have been presented in Paper I; see Atherton et al. (1982) and Bland & Tully (1989) for more detailed discussions. The narrow [S II] filters and small velocity range scanned allowed us to use the standard flat-fielding procedures, which was not the case for the HH 34 data in Paper I. The "white light" data cubes of individual flat fields taken at each etalon gap setting for each emission line were normalized to the maximum of the relevant filter transmission profile, and then divided into the data to remove variations in the pixel-to-pixel sensitivity as well as the filter transmission. Narrow emission rings arising from ambient Hα and [S II] emission were removed from the data by subtracting a median profile binned across the ring in a circle centered at the on-axis position. The ring subtraction was quite effective for these data because the ambient emission around HH 111 was reasonably uniform. The data cubes were then phase corrected to stacks of monochromatic images by calibrating the change in on-axis wavelength as a function of etalon gap using Ne-Ar comparison lines. The spectrophotometric standard star LTT 4364 was observed to convert CCD counts to absolute fluxes (Hamuy et al. 1992).

As with the HH 34 data in Paper I, HH 111 was observed at the same velocities in each line of the [S II] doublet and Hα to obtain complete spatial maps of the [S II] λ6716/λ6731 and [S II] (λ6716 + λ6731)/Hα line ratios. The background below ~2 σ of the mean sky was excluded when ratioing images, to restrict the analysis to bright regions.

3. RESULTS

The summed Hα and [S II] intensity maps of HH 111V working surface region are shown in Figure 1. The images have been rotated to align the jet axis along the vertical axis. East is approximately toward the top and north to the right. The regions labeled by Reipurth (1989a) are marked in the [S II] image. The images in Figure 1 (as well as in Figs. 3 and 4) are shown with the same spatial scale as their counterparts in Paper I for HH 34.

3.1. *Line Profile across the HH 111V Working Surface*

Spectral grids of the HH 111V working surface region are presented in Figure 2 for the Hα and [S II] (λ6716 + λ6731) emission lines. The data cubes consist of 13 velocity images in Hα covering a range from −135 to +45 km s^{-1} at 15 km s^{-1} intervals, and 11 velocities in each line of the [S II] doublet covering a range from −105 to +45 km s^{-1} also at 15 km s^{-1} intervals. These velocity ranges cover the full velocity extent of the emission in each of the lines observed—all of the profiles go nearly to zero intensity at each extreme.

3.2. *Electron Densities and Excitation Conditions*

The Fabry-Perot observations of HH 111 enable us to measure line ratios at each spatial position as a function of velocity. Hence, we can use the [S II] λ6716/λ6731 line ratio to measure electron densities (McCall 1984) and the [S II]/Hα ratio to determine the excitation state throughout the volume delineated by the working surface. Because the HH 111V working surface appears reasonably axisymmetric and is nearly in the plane of the sky (RRH), it is easier to interpret the

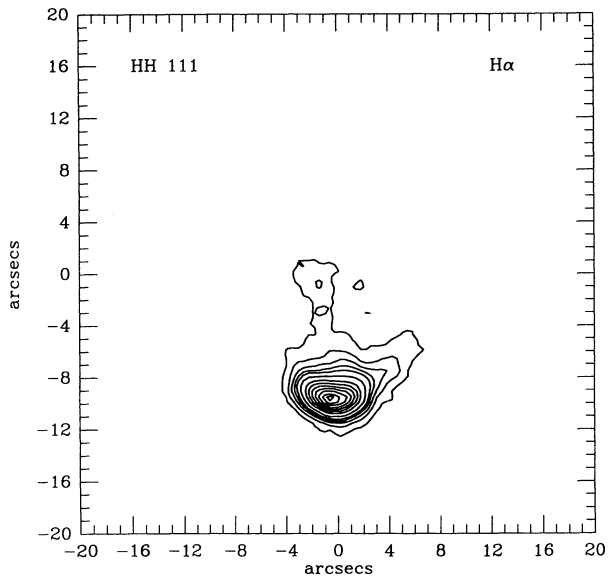

FIG. 1a

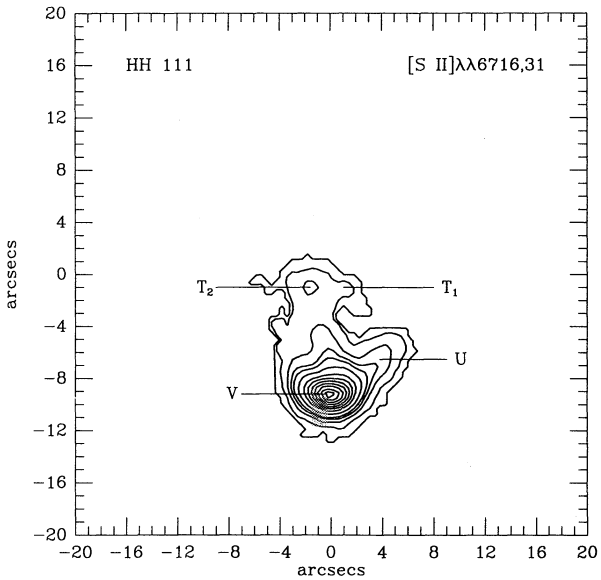

FIG. 1b

FIG. 1.—Images of the HH 111V working surface in the (*a*) Hα and (*b*) [S II] (λ6716 + λ6731) emission lines, summed over the individual velocity image for each line. The images have been rotated to make the jet axis vertical, with north approximately to the right and east to the top, and are presented (along with Figs. 3 and 4) at the same spatial scale as the corresponding images for HH 34 in Paper I. Contour levels are set to 4%, 8%, 12%, 16%, 20%, 28%, 40%, 50%, 60%, 70%, 80%, 90%, and 97% of the maximum intensity. The peak reddening-corrected surface brightnesses are 1.5×10^{-14} and 1.2×10^{-14} ergs s^{-1} cm^{-2} arcsec^{-2} for Hα and [S II], respectively. Note that these images result from summing over only a partial sampling of each emission line profile, so these peak surface brightnesses underestimate those that would be obtained through narrow-band images which completely sample the emission lines. The regions identified in the [S II] images are from Reipurth (1989a).

velocity dependence of the (bow shock) emission (see Hartigan, Raymond, & Hartmann 1987, hereafter HRH; Hartigan et al. 1990). Figure 3 (Plate 16) shows the average electron densities across the bow shock, obtained by taking the ratio of the *velocity-integrated* [S II] λ6716 emission to [S II] λ6731 emission at each point. Morphologically, Figure 3 demontrates how the postshock electron density varies as a function of shock velocity along the bow shock—the highest densities (orange and red) are found near the apex while there is a steady drop to low densities (blue) in the extreme bow shock wings. The total range of electron densities measured in the *monochromatic* images is from ~1800 cm^{-3} at the apex to ~250 cm^{-3}

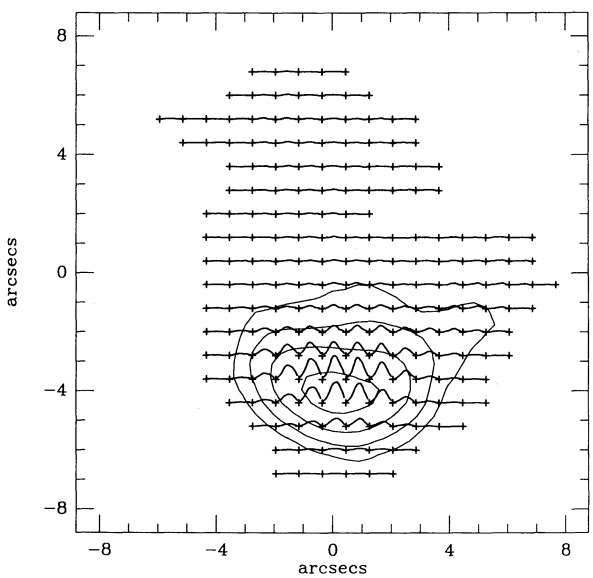

FIG. 2a

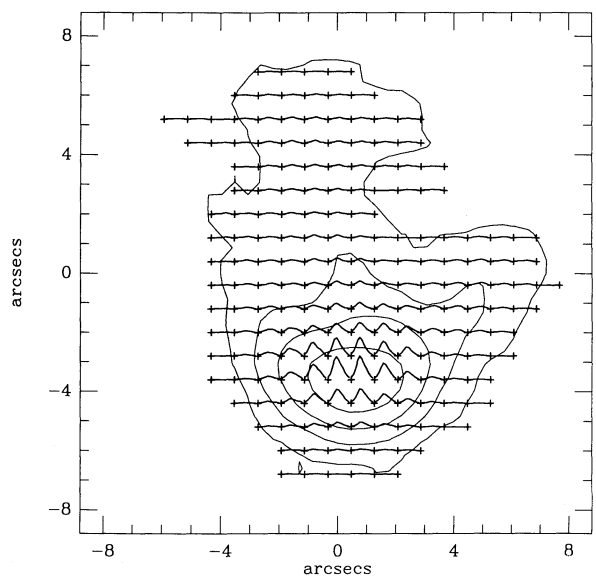

FIG. 2b

FIG. 2.—Spectral grids across HH 111V for the (*a*) Hα and (*b*) [S II] (λ6716 + λ6731) emission lines. To reduce confusion, only four underlying contours of the images from Fig. 1 are drawn, at 10%, 20%, 40%, and 80% of the maximum intensity. Each line profile is the sum of 2 × 2 pixels (0″.8 × 0″.8). The heliocentric velocity limits of the spectra for each line are Hα from −135 to +45 km s^{-1}, and [S II] from −105 to +45 km s^{-1}, with bluer wavelengths to the left. The profiles have been sampled at 15 km s^{-1} intervals in each emission line. The spectra are normalized to the maximum of the highest peak in each grid to preserve the relative intensities as a function of position across the working surface.

in the extreme bow shock wings, that is, almost covering the full dynamic range of the [S II] line ratio.

A map of the *average* [S II]/Hα ratios across the working surface is displayed in Figure 4 (Plate 16). The Hα emission dominates the apex and the regions close to the forward edge of the bow shock, while [S II] emission becomes relatively stronger away from the apex and farther up the wings. As with HH 34, the rise in the [S II]/Hα ratio from the apex to the extreme wings indicates the decreasing excitation as the perpendicular shock velocity decreases. The gradient across the bow shock wings from Hα-dominated emission along the forward edge to predominantly [S II] emission away from the edge tracks the radiative cooling behind the shock. The strong Hα emission arises chiefly from collisional excitation immediately behind the shock while the gradient to the [S II] dominated region shows the transition to the recombination zone where $T \lesssim 10^4$ K. This explanation was offered by RRH who noticed a clear spatial separation between the peak Hα and [S II] emission in the northern wing. Models by Raga & Binette (1991) have qualitatively matched the stratified structure of the postshock cooling region. However, as explained in § 4, we believe that the magnetic field extends the cooling distance, as it does in HH 34, so that the low-density preshock medium and very low shock velocity requirements in the models of Raga & Binette are no longer necessary.

3.3. *Fluxes and Reddening Correction*

The absolute fluxes for HH 111 data are somewhat uncertain because the order separation filters placed in front of the etalon passed continuum light from the standard star LTT 4364 in several spectral orders. We used the same Hα filter as for the HH 34 data. By convolving its transmission profile with the periodic Airy function of the etalon we estimate that $\sim 15\% \pm 5\%$ of the standard star flux at Hα was due to leakage from neighboring orders. The contamination in the [S II] filters used here was far less than for the HH 34 data, however, and the total line fluxes calibrated for the individual [S II] emission lines agreed with those derived by extrapolating from the Hα region.

We obtained the total line fluxes from HH 111V by summing the line profiles across the entire working surface for each of the lines observed. These Hα and [S II] line fluxes contain contributions from both the bow shock and Mach disk. The observed integrated Hα line flux is 3.8×10^{-14} ergs s^{-1} cm^{-2}, and the combined [S II] line flux is 4.2×10^{-14} ergs s^{-1} cm^{-2}. The uncertainty in the fluxes is $\sim 20\%$, due to uncertainties in measuring the total fluxes and the flux calibration.

We estimated the interstellar extinction toward HH 111V using the observed Hα/Hβ ratio in a low-resolution long-slit spectrum obtained for another program, assuming an intrinsic ratio of Hα/Hβ = 3. We failed to detect [O III] λ5007 in HH 111V in the long-slit spectrum and in a 600 s narrowband exposure, suggesting that the bow shock velocity cannot exceed ~ 100 km s^{-1} (see Cox & Raymond 1985; HRH). In § 4.1 we derive a bow shock velocity ~ 90–100 km s^{-1} based on the absence of [O III] emission and the observed [S II] and Hα emission distributions. Therefore, an intrinsic Hα/Hβ = 3 for the apex region of the bow shock is probably not in error by more than 10%, even if collisional excitation is important at the apex. The observed Hα/Hβ in HH 111V is 5.9 with an uncertainty of $\sim 10\%$. If we adopt the standard reddening law described by Cardelli, Clayton, & Mathis (1989), with $R_V = 3.1$, then adjusting the Hα/Hβ ratio from its observed value to 3 requires $A_V = 2.16 \pm 0.31$ and $E(B-V) = 0.70 \pm 0.10$. The corrected fluxes across the entire working surface for Hα and [S II] λλ6716, 6731 are 1.9×10^{-13} and 2.0×10^{-13} ergs s^{-1} cm^{-2}, respectively, ±30% due primarily to uncertainties in the intrinsic Hα/Hβ ratio and the flux calibration.

4. DISCUSSION

4.1. *Determination of the Shock Velocity and Bow Shock Shape*

In Paper I we estimated the bow shock velocity for HH 34 from the spatial distribution of the [O III] λ5007 emission, assuming that the perpendicular shock velocity was ~ 100 km s^{-1} at the position in the bow shock wings where [O III] ceased to be detected. Determining the bow shock velocity is not as straightforward in the case of HH 111V because there is no observed emission from lines such as [O III] λ5007 which have a well-defined cutoff shock velocity. In fact, in our low-resolution long-slit spectrum and narrow-band image of HH 111V, [O III] λ5007 was not detected down to a flux limit of about 1×10^{-17} ergs s^{-1} cm^{-2} $arcsec^{-2}$. Instead we use the absence of [O III] emission to set an upper limit to the shock velocity at the apex.

In the equilibrium preionization shock models of HRH, [O III] λ5007 emits strongly only for shock velocities $\gtrsim 100$ km s^{-1} because at lower shock velocities, the equilibrium conditions predict a significant neutral fraction of H and He entering the shock. Just behind the shock, there is a thin, high-temperature zone where the neutrals are ionized by collisional excitation, with the ionization of H and He occurring most rapidly. The net effect is to reduce the energy available to ionize the heavier ions (Cox & Raymond 1985). By contrast, [O III] λ5007 is a strong emitter in the fully preionized models of HRH down to a shock velocity of ~ 80 km s^{-1}. HRH found that assuming equilibrium preionization conditions in their bow shock models gave much better agreement with the observed emission line ratios in several HH objects than using full preionization. The use of equilibrium preionization is also borne out by the results presented for HH 34 in Paper I. Thus, if we assume equilibrium preionization conditions for HH 111V, we can establish an upper limit to the shock velocity at the apex of ~ 100 km s^{-1} based on the absense of [O III] emission.

As for a lower limit to the bow shock velocity, we note that because the Hα and [S II] emission-line widths in Figure 2 exceed 120 km s^{-1}, it is unlikely that the bow shock velocity is less than 80 km s^{-1} as required by full preionization conditions. In HH 34, the bow shock velocity we derived was $\sim 60\%$–70% of the observed [S II] and Hα velocity dispersions (see Paper I). We attributed the large line widths in HH 34 to thermal broadening by collisional excitation immediately behind the shock (for Hα; Raga & Binette 1991), the bow shock geometry (HRH), and unresolved turbulent motions in the postshock flow (Blondin, Fryxell, & Königl 1990). Additionally, the velocity dispersion for HH 111V is only slightly smaller than for the bow-shaped jet "knot" HH 111L (RRH), which does show a trace of [O III] emission and, therefore, has a shock velocity ~ 100 km s^{-1} (Morse et al. 1993).

Finally, we observe that the [S II] emission intensity drops markedly in Figure 1 at a radius of $\sim 2''.4$ from the axis of symmetry, while the Hα intensity drops off somewhat more gradually. Minima in the [S II]/Hα ratios are evident at this radius, though somewhat asymmetric with respect to the jet

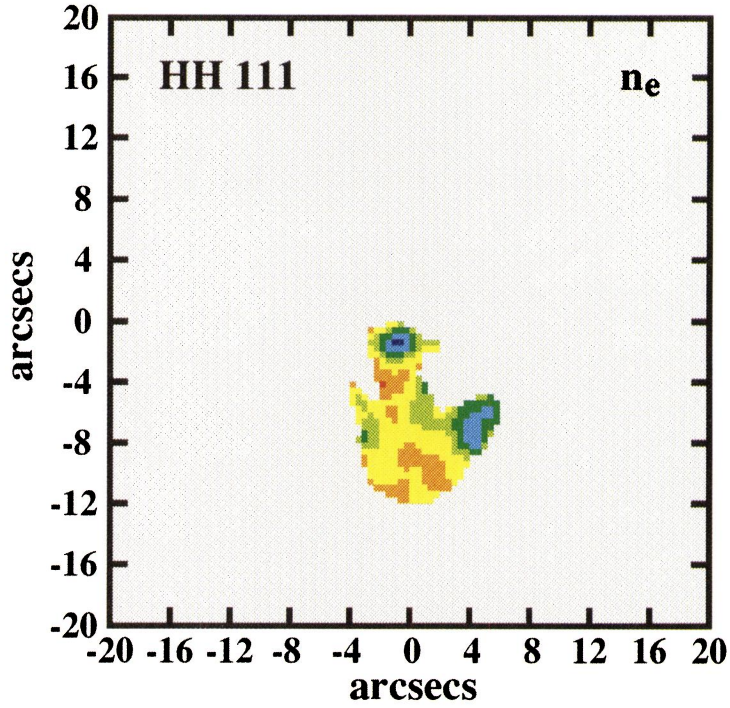

FIG. 3.—Map of average electron densities across HH 111V. The colors correspond to the following electron densities: blue, $n_e < 200$ cm^{-3}; light blue, $200 < n_e < 275$ cm^{-3}; dark green, $275 < n_e < 375$ cm^{-3}; light green, $375 < n_e < 500$ cm^{-3}; yellow, $500 < n_e < 650$ cm^{-3}; orange, $650 < n_e < 800$ cm^{-3}; red, $800 < n_e < 1000$ cm^{-3}. Note that in general the highest densities are found near the apex of the bow shock where the shock velocity is the highest, and the electron densities decrease to low values in the bow shock wings, particularly the northern wing, where the shock velocities are low.

MORSE et al. (see, 410, 766)

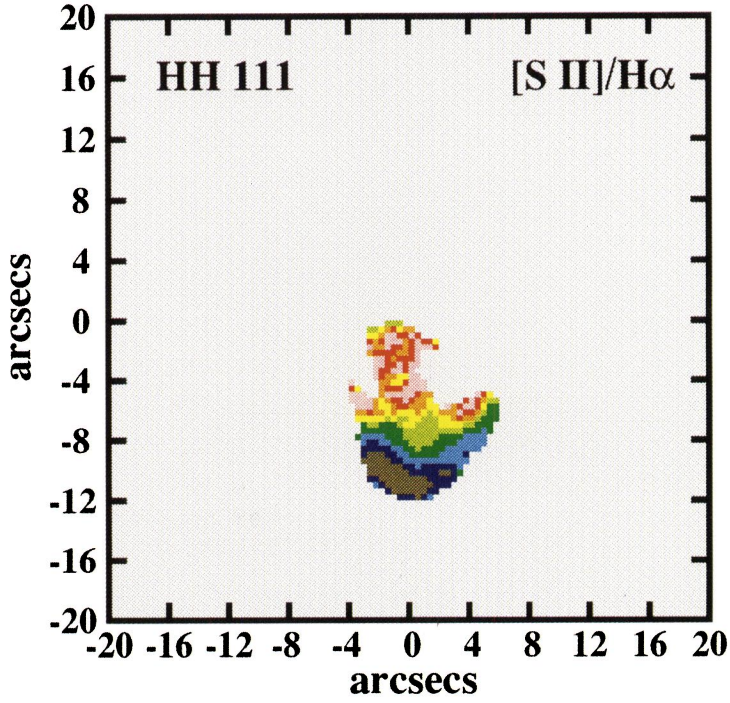

FIG. 4.—Map of average [S II]/Hα ratios across HH 111V. The colors correspond to the following values: dark gray, $0.40 <$ [S II]/Hα < 0.70; blue, $0.70 <$ [S II]/Hα < 0.95; light blue, $0.95 <$ [S II]/Hα < 1.10; dark green, $1.10 <$ [S II]/Hα < 1.35; light green, $1.35 <$ [S II]/Hα < 1.50; yellow, $1.50 <$ [S II]/Hα < 1.85; orange, $1.85 <$ [S II]/Hα < 2.10; red, $2.10 <$ [S II]/Hα < 2.40; lavender, $2.40 <$ [S II]/Hα < 3.20. In general, Hα dominates the emission near the leading edge of the bow shock, while [S II] is relatively stronger away from the leading edge.

MORSE et al. (see, 410, 767)

axis, in Figure 4. The left minimum occurs in the middle of the larger gray region, while the right minimum is the small island of gray embedded in dark blue. Below we show that such off-axis minima are predicted by our shock models, using equilibrium preionization, at perpendicular shock velocities of $\sim$60–80 km s^{-1} (see also HRH), and that these can be used to estimate the shock velocity at the apex of the bow shock. However, we stress that in this situation, our strongest constraints for a bow shock velocity in the range $80 < V_S < 100$ km s^{-1} are the absence of [O III] emission combined with a reasonably large velocity dispersion.

To further illustrate the effects of the preionization on the predicted line ratios, Figure 5 shows the fluxes of Hα, [S II] and [O III] and the [S II]/Hα ratio as a function of shock velocity that are predicted by planar shock models with a preshock density of 200 cm^{-3} and magnetic field of 30 μG—the values we later derive for HH 111V (see § 4.2).[3] Three preionization conditions are shown: full preionization, equilibrium preionization, and neutral incident gas. First, note the behavior of [O III] λ5007 in the lower right panel. This relatively high-excitation line increases in intensity at the higher shock velocities with increasing degree of preionization. The intensity quickly drops to zero below 100 km s^{-1} with equilibrium preionization conditions, as expected. In the upper left panel, the Hα flux is *greater* with the neutral incoming gas for high shock velocities because of the contribution of collisional excitation. Note how in the equilibrium models, the Hα curve crosses from the fully preionized curve to the neutral curve where the equilibrium conditions begin to predict a significant neutral fraction in the preshock medium. The [S II] flux in the equilibrium model also crosses from the preionized curve to the neutral curve at shock velocities below 100 km s^{-1}, but with a sharp *decrease* in the emitted flux. This inverse trend of the Hα and [S II] fluxes that occur when the neutral fraction becomes significant produces the minimum in the [S II]/Hα ratio seen in the lower left panel. A similar trend exists for the emissivities of other low-excitation ions relative to Hα, such as [Ca II]/Hα, [Si II]/Hα, etc. (see HRH). This trend will only occur in shocks when collisional excitation of H is important (see the fully preionized curve). Note that the model predicts values for the [S II]/Hα ratio through the minimum region between shock velocities 50–80 km s^{-1} that are a factor of $\sim$2 below the values indicated in Figure 4 (i.e., the models do not predict enough [S II] emission). This is somewhat due to Figure 4 showing average values along the line of sight, rather than the monochromatic values which agree slightly better with the models, but may also suggest that we have used an inappropriate abundance for S in the models (see § 4.2), or that one-dimensional models may not be perfectly applicable to this bow shock (see § 4.4).

The shock velocity at the apex can be estimated using equation (5) from Paper I. In HH 111V the critical velocity $V_\perp = V_c \approx 70$ km s^{-1} and radius $R = R_c \approx 2\farcs4$ correspond to the parameters assigned to the point where the [S II]/Hα ratio goes through a minimum in each bow shock wing. We fit the observed shape of the HH 111V bow shock with a simple

[3] The values of the fluxes and line ratios in Fig. 5 will change as n_0 and B_0 are varied, but the qualitative behavior of the curves as a function of preshock ionization will be the same.

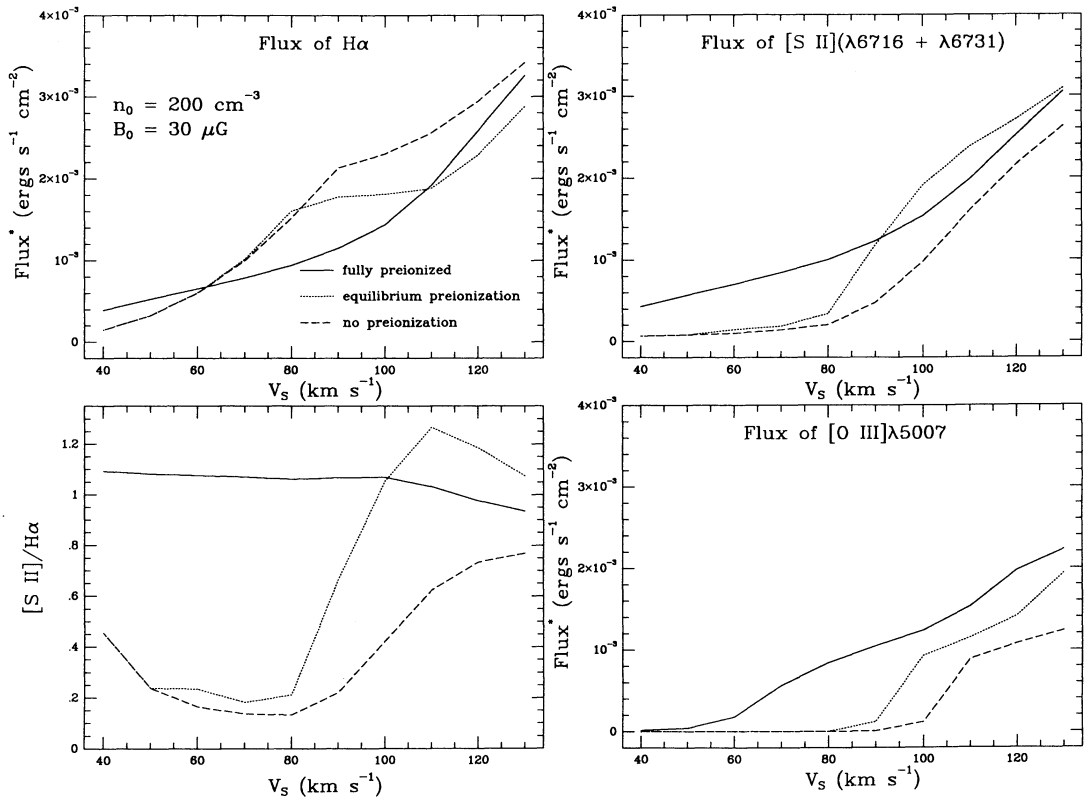

FIG. 5.—The fluxes of Hα, [S II] and [O III] and the [S II]/Hα ratios as a function of shock velocity predicted by planar shock models

parabola according to equation (1) from Paper I and derive $\alpha_0 = 0.2$ with an uncertainty of $\sim 5\%$. We use a value of $\phi = 80°$ for the inclination to the line of sight, as measured by RRH. Substituting these parameters into the equation for V_S yields a bow shock velocity of ~ 95 km s^{-1} with an uncertainty of about ± 20 km s^{-1} from uncertainties in R_c, V_c, α_0, and ϕ. A bow shock velocity of 95 km s^{-1} lies just below the upper limit of 100 km s^{-1} imposed by the lack of observable [O III] emission. We conclude that any likely correction to the bow shock velocity derived here should be toward a slightly lower shock velocity.

4.2. *Planar Shock Models for the HH 111V Bow Shock*

Our approach toward modeling the bow shock emission has been described in Paper I. The emission from a steady bow shock is locally approximated by one-dimensional calculations like those described in Raymond (1979), Cox & Raymond (1985), and HRH. Planar shock models were calculated over a range in shock velocity from 40 to 100 km s^{-1} at 10 km s^{-1} intervals in order to account for the variation of the perpendicular velocity, $V_\perp$, across HH 111V.

We estimated the preshock density, n_0, with equation (8) in Paper I by using the observed Hα flux at the apex of the bow shock, sampling the bright region inside the critical radius $R_c \approx 2''.4$ over which the estimated shock velocities range from ~ 95 km s^{-1} at the apex to ~ 70 km s^{-1} at R_c. The reddening-corrected Hα flux from the apex region is $F_{H\alpha} \approx 1.1 \times 10^{-13}$ ergs s^{-1} cm^{-2}. A distance, d, to HH 111 of 460 pc is assumed (Reipurth 1989b). The cross-sectional area for the emitting surface is $\sigma_c = \pi R_c^2 \approx 18$ arcsec$^2 \approx 8.6 \times 10^{32}$ cm^2. The mean shock velocity weighted over the emitting area is $V_{ap} \approx 85$ km s^{-1}. Finally, a value of $f_{H\alpha} \approx 0.66$ was used for the number of Hα photons produced per H atom. Inserting these parameters into the equation for the preshock density yields $n_0 \approx 200 \pm 100$ cm^{-3}, where the error accounts for the uncertainties in R_c, V_c, $f_{H\alpha}$, the absolute flux, and the effective shock velocity.[4]

The relatively low shock velocity for HH 111V implies that the ultraviolet radiation produced at the apex of the bow shock does not ionize the preshock gas entering the bow shock wings significantly. Thus, we assumed no modification to the equilibrium preionization conditions, as tabulated in HRH, in the models. We fixed the logarithmic abundance ratios for H:He:N:O:Ne:S:Ar:Fe:Ni to the values reported by Osterbrock, Tran, & Veilleux (1992) of 12.00:11.00:7.72:8.49:7.60:6.97:6.41:6.43:5.15 for the Orion Nebula region. There is no guarantee that these metal-poor abundances should apply to the HH 111 region, at a projected distance of ~ 80 pc from the Orion Nebula. However, in our long-slit spectrum of HH 111 (Morse et al. 1993), the low [N II]/Hα and [O II]/Hα line ratios, and the relative weakness of all observed Fe lines, suggest that the Orion abundances are more appropriate. Unfortunately, the [S II]/Hα ratios in the planar shock models are more sensitive to the preionization conditions (see Fig. 5) than to abundance changes over the shock velocities of interest, so it is impossible to contrain the abundances from this one line ratio without a definite knowledge of the preionization. If the refractory elements are highly depleted, as suggested by the Orion iron abundance, the main effect on the models will be a modest reduction in the cooling rate, particularly below 10^4 K. The abundances for C:Mg:Si:Ca, which were not measured by Osterbrock et al., were set to the "cosmic" values of 8.52:7.42:7.52:6.30 (Allen 1973).

The preshock temperature was always taken to be 10^4 K in the models. A radiative transfer parameter R_{max} (Cox 1972; Raymond, Hartigan, & Hartmann 1988) was taken to be 1, appropriate for the nonplanar geometry of a bow shock. Calculation of the emission-line fluxes was terminated either when the gas temperature cooled below 1000 K or the cooling time exceeded 800 yr, approximately the dynamical lifetime of the HH 111V bow shock (RRH). Small step sizes were used in the calculations to sample adequately the postshock temperatures near 10^4 K where the gas becomes optically thick to Lyman-continuum photons. We assumed equal electron and ion temperatures throughout the flow. If only Coulomb collisions act to transfer energy between electrons and ions, the electron temperature will be significantly below the ion temperature in much of the postshock gas, and the emergent spectrum will resemble that of a somewhat slower (by ~ 10–20 km s^{-1}) shock (Ohtani 1980). In the absence of definite knowledge of the degree of electron-ion equilibration by plasma turbulence, we assumed $T_e = T_i$, and point out that slightly higher shock velocities may be needed to match the observed line ratios if only Coulomb collisions operate.

We constrained the preshock magnetic field, B_0 ($= B_\perp$), by comparing the compression across the HH 111V bow shock to the compression predicted by shock models with B_0 ranging from 0.1 to 100 μG. We define the compression, X, as the ratio of the postshock electron density, as measured by the [S II] λ6716/λ6731 ratio, to the preshock density, n_0, in both the data and the models. The results of the comparison are shown in Figure 6. The HH 111V data were averaged from the individual velocity images as a function of position and velocity along each side of the bow shock. The points for the lowest shock velocities (< 60 km s^{-1}) were taken from positions along the northern wing (righthand side in Fig. 1). The individual measurements are marked by the open boxes and are connected by the solid line. The compressions measured in the models are shown by the dotted curves. The error bars assigned to the data points in the top plot account for the statistical uncertainties in the measured electron densities. These uncertainties increase toward lower shock velocities due to a decrease in the signal-to-noise of the data toward the extremes of the bow shock wings. The error bars in the bottom plot incorporate the uncertainty in the estimated preshock density, which is a systematic error that affects all the data points in the same way. Because the measured electron densities are fixed, altering the preshock density moves all the points in the solid curve up or down by the same amount. Note that the dotted curves in the bottom plot will move in the same direction as the solid curve as the preshock density is varied by $\pm 50\%$.

The compression curve in Figure 6 indicates that B_0 is ~ 30 μG. This is a factor ~ 2–3 times greater than that found for HH 34 in Paper I. Magnetic fields several times this value have been measured at the edges of molecular clouds (e.g., Vallée 1989) though typically in much higher density environments. The flattening out of the HH 111V compression curve at lower shock velocities may arise from a density gradient in the preshock medium that increases toward the northern wing. Such a gradient would enhance the emission in the northern wing compared to the southern wing. We note that if a coherent large-scale ambient B field was aligned along the HH 111 jet

[4] Note that the equation for the preshock density actually does not depend on the distance to HH 111, because the d^2 in the numerator is canceled by a similar factor in converting σ^2 to cm^2 in the denominator.

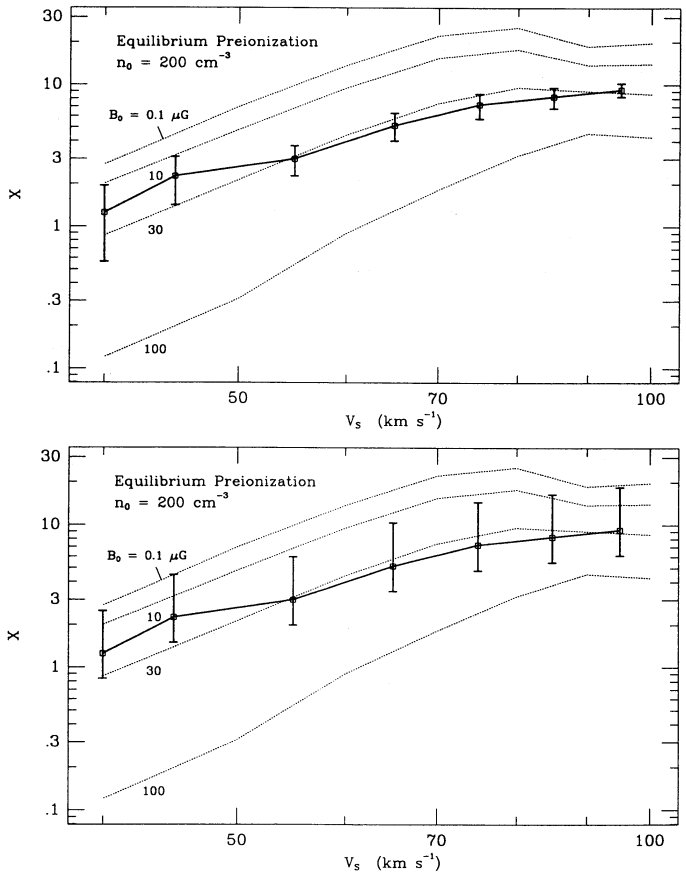

FIG. 6.—A comparison of the compression across the HH 111V bow shock to the compression predicted by shock models computed over a range in B_0 from 0.1 to 100 μG. The compression, X, is defined as the ratio of the post-shock electron density, as measured by the [S II] λ6716/λ6731 ratio, to the preshock density, n_0, in both the data and the models. The HH 111V data were averaged from the individual velocity images as a function of position and velocity along each side of the bow shock. The points for the lowest shock velocities (<60 km s^{-1}) were taken from positions along the northern wing (righthand side in Fig. 1). The individual measurements are marked by the open boxes and are connected by the solid line. The compressions measured in the models are shown by the dotted curves. The error bars assigned to the data points in the top plot account for the statistical uncertainties in the measured electron densities. The error bars in the bottom plot account for the uncertainty in the preshock density, which is a systematic error that affects all the data points in the same way.

axis, we should see very high compressions at the apex of the bow shock (where the compression would be unaffected by the field) and very low compressions in the wings (where the field would inhibit the compression) relative to any of the particular model compression curves—that is, no single B_0 could be used in the models to map the compression along the bow shock as the orientation to the ambient B field changed from the apex to the wings. Because the $B_0 \sim 30$ μG compression curve does closely mimic the observed compression curve, we conclude that our data suggest no special orientation of the jet axis to any large-scale B field, and that the B field may be turbulent over scales the size of the bow shock.

The predicted emission-line fluxes, normalized to the flux of Hβ = 100, from the planar shock models using the Osterbrock et al. (1992) Orion abundances are given in Table 1. The preshock ionization, n_0 and B_0 for each shock velocity are also indicated, along with the computed cooling times and distances.

4.3. *The Bow Shock Model for HH 111V*

We modeled the bow shock emission with the bow shock code described in Paper I and HRH. A three-dimensional bow shock was created from the observed shape and estimated shock velocity of HH 111V (§ 4.1), and the emission interpolated among the planar shock models in Table 1. The model assumes that the emission is confined to an unresolved paraboloidal surface around the axis of symmetry and thus will not predict any spatial displacement between the [S II] and Hα emission (Fig. 4; RRH) that is caused by a resolved cooling distance. The bow shock was projected onto the sky at a viewing angle $\phi = 80°$. Monochromatic images were generated and smoothed spatially by a Gaussian seeing profile of 1.″3 FWHM, to approximate the observing conditions. The line profiles were smoothed by a Gaussian with width due to the combination of thermal motions of the emitting gas and the instrumental broadening (35 km s^{-1} FWHM). Because collisional excitation is important for the Hα emission over the whole bow shock, two separate emitting bow shocks were generated, one containing emission from collisional excitation and the other from recombination. The line profiles in the collisionally excited bow shock were smoothed by a Gaussian with width generated by gas at $T \approx 1.5 \times 10^5$ K, whereas $T \sim 10^4$ K was used for the recombination bow shock. After smoothing, the two Hα bow shocks were summed. We assumed a temperature of 10^4 K to smooth the [S II] model. Figure 7 shows a comparison of the projected emission distributions of the data and the bow shock models in [S II] and Hα.

We compare our observed (solid lines) and predicted (dotted lines) spectral grids in Figure 8. The velocity limits of each spectral bin are the same as in Figure 2. The match between the observed and predicted velocity fields appears somewhat better here than for HH 34, owing to the more axisymmetric appearance of HH 111V, though the model predicts substantially more emission from the extreme bow shock wings than is observed. The added smoothing of the model Hα line profiles due to the high temperature of the collisionally excited gas also

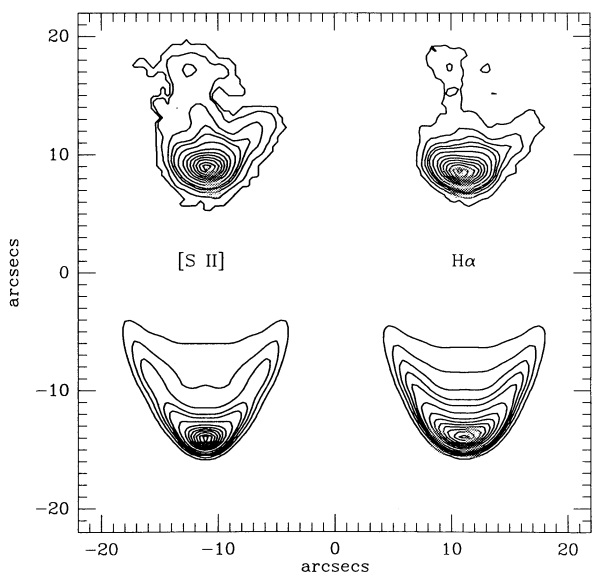

FIG. 7.—A comparison of the projected emission distributions of the data and the bow shock models in [S II] and Hα.

TABLE 1

PREDICTED EMISSION-LINE FLUXES IN HH 111V FROM PLANAR SHOCK MODELS WITH ORION ABUNDANCES

MODEL	S100	S090	S080	S070	S060	S050	S040
V_S (km s^{-1})	100	90	80	70	60	50	40
X (H I)	0.31	0.62	0.92	0.97	0.99	1	1
Y_0 (He I)	0.66	0.95	1	1	1	1	1
Y_1 (He II)	0.34	0.05	0	0	0	0	0
n_0 (cm^{-3})	200	200	200	200	200	200	200
B_0 (μG)	30	30	30	30	30	30	30
T_{800} (K)	1000	1000	1000	1000	1000	1000	1000
d_{c4} (AU)	9.8	7.4	2.7	2.2	2.7	5.1	12.4
d_{c3} (AU)	311	272	159	148	184	275	506
τ_{c4} (yr)	7.4	6.7	3.2	2.5	3.1	5.5	12.7
τ_{c3} (yr)	459	406	239	222	273	402	716
$F_{H\beta}$ [1]	6.25	6.22	5.30	3.23	1.85	.940	.390
He II 304	2830	74.3	1.3	0.4	0.1	0	0
C III 977	1610	436	7.0	2.0	1.0	1.8	0.4
N III 991	75.3	14.7	0.1	0	0	0	0
S III 1198	98.8	50.4	1.7	0.7	0.5	1.1	0.9
Si III 1206	336	201	2.2	0.7	0.3	0.1	0
Ly α 1216	5296	5482	6300	6693	7192	7956	9433
C II 1336	373	252	12.3	10.3	10.6	10.8	17.4
Si IV 1397[2]	188	27.4	0.1	0	0	0	0
O IV] 1402[3]	16.9	0	0	0	0	0	0
N IV] 1486	9.8	0.1	0	0	0	0	0
C IV 1549	419	6.4	0	0	0	0	0
He II 1640	11.9	0.2	0	0	0	0	0
O III] 1663[2]	78.4	8.9	0	0	0	0	0
N III] 1750[3]	36.1	9.0	0.1	0	0	0	0
Si III] 1891	188	147	3.0	0.7	0.3	0.1	0
C III] 1908	613	259	13.4	4.5	2.4	5.0	1.7
N II] 2141[2]	10.8	10.7	1.3	0.9	0.9	1.0	1.3
C II] 2326[3]	415	256	37.1	29.5	32.9	41.2	72.9
Si II] 2340[3]	23.4	11.6	4.6	3.5	3.8	5.0	7.9
[Ne IV] 2423[2]	3.7	0	0	0	0	0	0
[O II] 2470	28.0	27.5	4.0	1.8	1.0	0.7	0.4
Mg II 2799[2]	491	160	42.6	41.1	46.4	34.8	58.1
Mg I 2852	47.8	21.2	4.6	3.0	3.3	2.8	7.9
[O II] 3726	250	209	52.9	30.6	22.3	16.9	12.4
[O II] 3729	147	128	31.0	20.7	18.5	17.5	15.7
[Ne III] 3869	21.8	9.5	0.6	0	0	0	0
Ca II 3945[2]	216	105	29.3	17.3	17.7	22.6	34.5
[Ne III] 3968	6.9	3.0	0.2	0	0	0	0
[S II] 4072[2]	40.5	23.9	5.8	4.5	4.6	3.3	6.3
Ca I 4227	7.2	5.7	2.7	1.7	1.8	2.3	3.4
[O III] 4363	12.6	1.5	0	0	0	0	0
[Fe III] 4658	1.1	0.9	0.2	0	0	0	0
Hβ 4861	100	100	100	100	100	100	100
[O III] 4959	50.6	6.6	0	0	0	0	0
[O III] 5007	147	19.1	0	0	0	0	0
[N I] 5200[2]	39.3	18.5	5.9	5.5	8.5	15.6	34.1
[N II] 5755	4.2	3.1	0.7	0.5	0.5	0.6	0.7
He I 5876	20.1	11.8	1.5	0.8	0.5	0.3	0.1
[O I] 6300	116	46.9	16.4	17.4	25.4	40.6	73.0
[O I] 6363	38.5	15.6	5.5	5.8	8.5	13.5	24.3
[N II] 6548	62.4	34.8	13.3	9.8	10.1	11.1	12.1
Hα 6563	289	285	302	313	327	344	378
[N II] 6583	185	103	39.4	29.1	29.7	32.9	35.7
He I 6678	7.5	5.3	0.7	0.4	0.3	0.1	0.1
[S II] 6716	130	79.8	26.7	25.0	36.4	42.9	96.5
[S II] 6731	175	109	37.1	32.2	40.3	39.3	75.3
[Ca II] 7307[2]	40.7	23.7	7.8	4.9	5.3	6.9	10.7
[O II] 7320	20.7	20.3	3.0	1.3	0.8	0.5	0.3
[O II] 7331	16.7	16.4	2.4	1.1	0.6	0.4	0.3
[Fe II] 8617	0.9	0.4	0.1	0.1	0.2	0.2	0.4
[C I] 8727	6.9	4.2	2.4	2.2	2.3	2.6	3.4
[S III] 9069	20.1	6.6	4.0	3.0	3.2	8.7	10.5
[S III] 9532	52.2	17.0	10.5	7.7	8.2	22.6	27.2
[C I] 9823	33.3	24.3	19.8	24.0	27.0	31.6	39.4
[C I] 9850	98.7	71.9	58.5	70.9	80.0	93.4	117
[S II]10289,339[2]	14.2	8.4	2.0	1.6	1.6	1.2	2.2

TABLE 1—*Continued*

MODEL	S100	S090	S080	S070	S060	S050	S040
[S II]10323,373[2]	12.9	7.6	1.9	1.4	1.5	1.1	2.0
[N I]10402[2]	6.2	2.6	0.8	0.6	0.6	0.8	1.2
He I 10830	30.7	22.5	2.2	1.3	0.9	0.6	0.3
[Ne II] 12.8μ	35.6	20.7	9.0	10.5	14.2	23.3	39.7
[Ne III] 15.6μ	19.9	6.9	1.2	0.4	0.2	0.2	0.1
[Si II] 35.3μ	300	226	152	191	302	541	1090
[O I] 63.2μ	49.5	30.5	16.6	18.8	27.6	44.5	84.0
2 photon	718	630	998	1204	1482	1894	2718

NOTE.—All fluxes are normalized to Hβ = 100. The parameters X, Y_0, and Y_1 refer to the ionization state of the preshock gas; n_0 is the preshock density; B_0 is the preshock magnetic field strength; d_{c4} and d_{c3} are the distances between the shock and the position where the postshock temperature $T = 10^4$ K and $T = 10^3$ K, respectively, while τ_{c4} and τ_{c3} are the corresponding cooling times; T_{800} refers to the postshock temperature reached when calculation of the emission-line fluxes was terminated, which was limited to a maximum cooling time of 800 yr.

[1] Flux of Hβ in units of 10^{-4} ergs s^{-1} cm^{-2} through *front* of shock.

[2] Line is a doublet.

[3] The $^4P - {}^2P$ intersystem transitions consist of five closely spaced lines (Mendoza 1983). There are seven lines of O IV] and Si IV] between 1393 and 1407 Å.

improves the agreement. Using the lower temperature alone to smooth the predicted profiles results in double-peaked profiles through the interior of the bow shock that are not observed. The [S II] line profiles are well matched at the apex and along the northern wing, but there is considerable emission through the interior of the bow shock that is not predicted by the model. We elaborate on this point in § 4.4.

To align the observed and predicted velocity fields, we had to shift the predicted line profiles by $\sim -30 \pm 15$ km s^{-1}, corresponding to an offset from the systemic velocity of the system (+23 km s^{-1}; RRH) of $\sim -53 \pm 15$ km s^{-1}. When scaled by the cosine of the viewing angle $\phi \approx 80°$, this shift implies that HH 111V is moving into a medium which already has a velocity of $\sim 305 \pm 85$ km s^{-1} away from the stellar source. Such a scenario would account for the large spatial motions ($\sim$400 km s^{-1}; see RRH) but low shock velocity ($\sim$95 km s^{-1}; see § 4.1) and agrees with the suggestion of Reipurth (1989a) that the HH 111 system is an episodic outflow. HH 111V apparently moves into the wake of a previous—and very powerful—ejection, as has been suggested for the HH 34 (Paper I; Heathcote & Reipurth 1992) and HH 46/47 (Hartigan et al. 1990; Reipurth & Heathcote 1991) systems. It is somewhat puzzling that there is no evidence for a previous ejection in the emission-line CCD images of RRH, though if the density of the undistributed medium were low and the shock velocity high, the initial bow shock may be nonradiative.

The ram pressure of the preshock gas of HH 111V is $\rho V^2 \approx 3.0 \times 10^{-8}$ ergs cm^{-3}, using $V = 95$ km s^{-1} and $\rho = 200 \times (1.67 \times 10^{-24})$ g cm^{-3}. The magnetic pressure in the preshock gas is $\sim B^2/8\pi \approx 3.6 \times 10^{-11}$ ergs cm^{-3}, using $B = 30$ μG (§ 4.2), or $\sim 10^{-3}$ times smaller than the ram pressure. Hence, the preshock field is not strong enough to divert the flow in front of HH 111V, the wake of the previous ejection(s). The density and magnetic field behind the below shock should increase by the compression ratio X, a factor of $\sim$10 at the apex (see Fig. 6). The magnetic field now contrib-

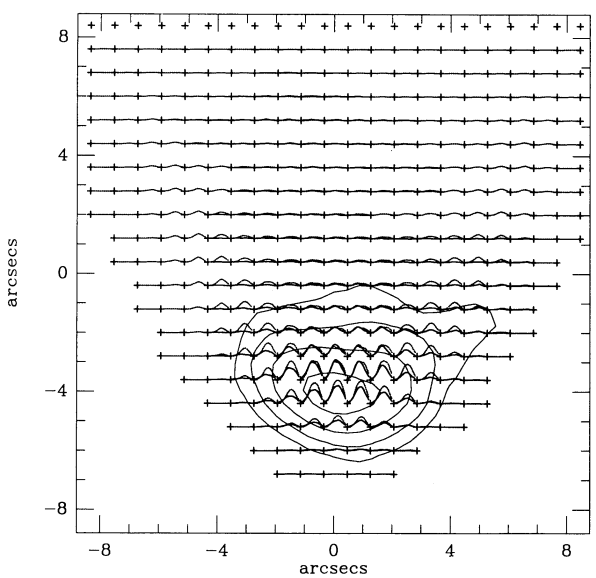

FIG. 8*a*

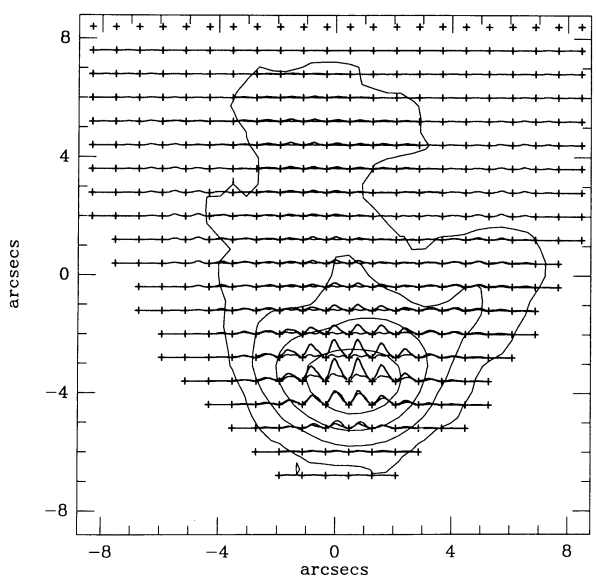

FIG. 8*b*

FIG. 8.—Observed (*solid lines*) and theoretical (*dotted lines*) spectral grids overplotted for (*a*) Hα and (*b*) [S II] (λ6716 + λ6731). The model has been shifted −30 km s^{-1} in radial velocity to align with the data, and the spectra profiles are plotted with the same velocity limits as in Fig. 2.

utes significantly to the total pressure in the postshock gas (comparable to the thermal pressure in the emitting region at $T \approx 10^4$ K), and the magnetic pressure reduces the compression that would occur if no magnetic field was present by a factor of ~ 2. Subsequently, the postshock cooling distance is extended by an order of magnitude versus a nonmagnetic shock (e.g., compare the cooling distances in Table 1 to the nonmagnetic shock models in HRH). While the magnetic field is unimportant ahead of the bow shock, B becomes dynamically important in the postshock flow by inhibiting the compression.

4.4. *Identification of the Mach Disk*

The Mach disk of HH 34 was relatively easy to isolate in the Fabry-Perot data presented in Paper I because it was spatially and kinematically distinct from the bow shock, had a high [S II] flux, and its low electron density and low excitation characteristics were indicative of a weak shock that was separate from the bow shock. The situation in HH 111V is apparently not as straightforward, however.

RRH obtained [S II] and Hα emission-line images of HH 111 in ~0".8 seeing with the ESO 3.5 m New Technology Telescope. They then partially deconvolved their images using the methods described in Raga & Mateo (1988) to an effective seeing disk of ~0".4. They showed in their Hα–[S II] image that the leading edge of the bow shock was dominated by Hα emission while the regions behind the bow shock, back toward the stellar source, were dominated by low-excitation [S II] emission. Although our F-P data do not have such high spatial resolution as the NTT images of RRH this behavior can also be seen in Figure 4. RRH interpreted the stratified emission structure in the northern bow shock wing as a cooling distance effect, but at the apex they preferred a bow shock/Mach disk scenario.

RRH supposed that HH 111V moved into a stationary medium and hence assumed that the shock velocity was ~390 km s^{-1} as implied by the large proper motion of HH 111V. The shock is then so strong, near its apex, that it would emit sufficient ultraviolent radiation to completely ionize the preshock gas. The Hα emission would, therefore, come primarily from the postshock recombination region. In this case RRH claimed, based on the calculations of Raga & Binnete (1991), that the strongest [S II] emission should then be seen *closer* to the shock than the Hα peak. Hence, they concluded that the stratified emission structure at the apex could not be explained as a resolved cooling zone and must instead correspond to the detection of emission from the bow shock at the leading edge and from the Mach disk in the trailing zone ~0".9 behind the apex.

We believe that there are two flaws in this argument. Firstly, for a shock velocity of ~400 km s^{-1} at the apex of the bow shock, HRH calculated a cooling distance of ~7000 AU, or $\sim 10^{17}$ cm, corresponding to over 10" at the distance of HH 111. But more pertinent to the present situation, in §§ 4.1 and 4.2 we presented evidence based on the absence of [O III] emission and the spatial emission distributions of [S II] and Hα that the shock velocity of HH 111V is instead only ~95 km s^{-1}. In this case the gas entering the shock contains a significant fraction of neutrals, implying that emission from the collisional excitation zone immediately behind the shock *dominates* the Hα light *even at the apex*. Hence the strongest Hα emission should lie closer to the shock than [S II] over the entire bow shock. The close match between the bow shock model and the data in Figure 8 supports this conclusion. A dominant contribution by collisionally excited Hα emission coming from a thin, unresolved shell immediately behind the shock is well approximated by our bow shock model when the thermal broadening is taken into account.

Second, even if the preshock gas were almost completely ionized, the maximum [S II] emission *only* lies ahead of the maximum Hα emission if the shock velocity is less than 80 km s^{-1}, where the postshock temperature is below $\sim 10^5$ K (Raga & Binnette 1991 only considered such low-velocity shocks). For shock velocities $\gtrsim$80 km s^{-1}, the recombining gas at $\sim 10^4$ K is reionized by Lyman-continuum photons produced in the hot region ($T \gtrsim 10^5$ K) immediately behind the shock. The gas is reheated, forming a temperature plateau at ~8000 K in which electrons are produced that collisionally excite most of the observed [S II] emission. Thus, in fast shocks with full preionization, the maximum [S II] emission, which is formed primarily at ~8000 K, *will not* be observed closer to the shock than Hα, which is formed primarily at $\sim 10^4$ K. In slower shocks, the temperature is too low to generate enough Lyman-continuum photons to reionize the cooling gas. In this domain, the [S II] emission comes from recombination at ~12,000 K. Only under these very special circumstances—fully ionized preshock gas but a low-velocity shock—will the brightest [S II] emission be closer to the shock than Hα. We thus believe that the stratification cross the entire bow shock HH 111V can be explained as a cooling distance effect. In addition, as in our discussion of the HH 34 cooling distance in Paper I, note that the one-dimensional cooling distances given in Table 1 are not appropriate by themselves since some fraction of the parallel velocity component is conserved across the bow shock, even near the apex, which will carry the postshock gas much further along than the one-dimensional cooling distances indicate. Emission-line ratio maps produced by a suitable two- or three-dimensional MHD code that can be compared with Figure 4 are necessary to resolve this issue.

Although much of the fine structure observed by RRH at the apex is unresolved here, the electron densities across the entire apex region in Figure 3 are the highest in the bow shock, while the [S II]/Hα ratios in Figure 4 increase gradually from the apex back. These characteristics are consistent with the emission rising from compressed gas that cools behind a strong shock. We also point out that the magnetic field present will extend the postshock cooling distances (see the discussion at the end of § 4.3).

We now consider the location of the Mach disk associated with HH 111V. In the steady state model, the Mach disk has the same velocity as the bow shock with respect to the stellar source. Hydrodynamical simulations (e.g., Blondin et al. 1989) show, however, that the Mach disk is a variable structure whose velocity with respect to the bow shock varies over long time scales. To first order though, we may expect that the Mach disk in HH 111V, if visible, can be kinematically associated with emission from the apex of the bow shock. Such was the situation for the Mach disk in HH 34 (Paper I).

Monochromatic [S II] images at three heliocentric velocities are shown in Figure 9: the left image at a very blueshifted velocity of −90 km s^{-1}; the middle at −45 km s^{-1}, roughly at the maximum intensity of the apex emission; and the right at +15 km s^{-1}. The intensities in the images have been normalized to the maximum of the bright −45 km s^{-1} slice. The appearance of these images can be interpreted with the position-velocity diagrams of Hartigan et al. (1990), especially

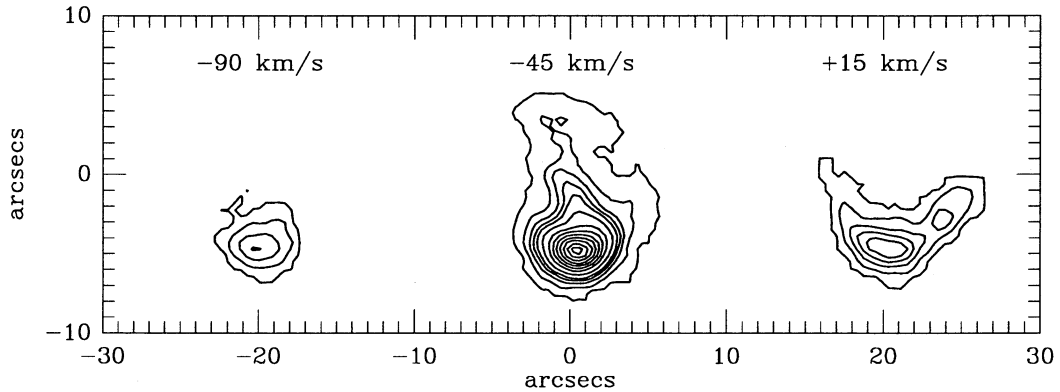

FIG. 9.—Monochromatic [S II] images of HH 111V at three heliocentric velocities: the left image at the very blueshifted velocity of -90 km s^{-1}; the middle at -45 km s^{-1}, roughly at the maximum intensity of the apex emission; and the right at $+15$ km s^{-1}. The intensities in the images have been normalized to the maximum of the bright -45 km s^{-1} image, and the contours are set to the same relative levels as in Fig. 1.

that for a viewing angle of $\sim 75°$. The -90 km s^{-1} image comes from a position in the bow shock close to the apex but on the near side facing us. The absence of wings is due to the inclination of the bow shock to the line of sight. The -45 km s^{-1} image is slightly blueshifted from the systemic radial velocity. It includes emission from the apex of the bow shock and ought to include emission from the Mach disk as well. We note the conspicuous presence of knot T, which lies exactly along the jet axis, and the bridge of emission connecting knot T to the bow shock V. Finally, the $+15$ km s^{-1} image traces the redshifted emission along the far side of the bow shock from just behind the apex up the limb-brightened wings. Note that the southern wing, though fainter than the northern wing, is readily apparent and reasonably symmetric about the jet axis. These data leave little doubt as to the bow shock nature of HH 111V.

Emission from the elongated knot T and the bridge from T to the bow shock can be kinematically associated with emission from the apex of the bow shock. This emission either comes from clumps in the foreground bow shock wing (see the long tail of emission in the p-v diagrams of Hartigan et al. 1990), or from within the jet. Unfortunately, with HH 111 being nearly in the plane of the sky, we cannot kinematically distinguish between these two scenarios with certainty. Knot T and the bridge are very low excitation regions in Figure 4 ([S II]/H$\alpha > 3$ in the monochromatic images), however, they differ quite dramatically in the electron density map of Figure 3. Electron densities in knot T are in the low-density limit (< 200 cm^{-3}), whereas in the bridge they reach ~ 2000 cm^{-3} in one clump, among the highest in the region. There is a slight velocity gradient along the bridge between knot V, where the velocity is ~ -45 km s^{-1}, to knot T, at ~ -35 km s^{-1}. Interestingly, knot T and the bridge are only marginally detected in the NTT images of RRH, do not show up in their Hα–[S II] image, and thus are not mentioned in their discussion. This may be due to poorer signal-to-noise relative to the F-P data.

If emission from knot T and the bridge arises in the foreground bow shock wing—that is, if HH 111 were rotated 90°, knot T and the bridge might appear like the northern wing—this implies that the preshock medium is very inhomogeneous, and that we are viewing the bow shock at a special orientation. The scale of this putative wing would be nearly twice as long as the northern wing, however, and electron densities would be very high compared to the northern wing, except in knot T itself, even though the perpendicular shock velocity was dropping swiftly. On the other hand, if the emission comes from shocks within the jet, knot T may represent the Mach disk, which decelerates the impinging jet material, or perhaps another "low-shock-velocity jet knot" which is in the process of overtaking knot V. The "jet knot" scenario for knot T seems unlikely because the radial velocity of the emission in knot T is lower than the mean velocity for knot V, and also implies that we are viewing HH 111 at a special time.

We conclude that knot T is a likely candidate for the Mach disk associated with the HH 111V bow shock. Emission from knot T and the bridge probably arise from regions along the jet axis several arcseconds upstream from the bow shock toward the stellar source. Knot T has the low excitation spectrum and the low electron densities indicative of a weak shock that is separate from the bow shock, similar to the situation in HH 34. Our conclusion is inconsistent with RRH's identification of the Mach disk $< 1''$ behind the apex of the bow shock.

Still, we need to explain the large excess of [S II] flux compared to the bow shock model through the interior of the bow shock and along the bridge to knot T. We note that if the (three-dimensional) cooling distance approaches the radius of curvature of the bow shock, as we suspect may be the case for HH 111V, modeling the emission in the recombination zone behind the bow shock by one-dimensional plane-parallel models is inappropriate. The emission in this limit must be modeled with an appropriate two- or three-dimensional MHD code (e.g., Stone, Mihalas, & Norman 1992). The excess emission may also arise from post-Mach disk gas, and so would not be predicted by the bow shock model. The excitation conditions in knot T indicate a weak shock (~ 20–40 km s^{-1}) that may have a very long cooling length, depending on the jet density and any possible magnetic field. The ensemble of knot T + the bridge + the bright, dense interior [S II] region may resemble the structure seen in, for instance, the three-dimensional simulations of overdense jets by Gouveia Dal Pino & Benz (1993), where several jet radii upstream from the bow shock, the flow is decelerated and recollimated by a weak internal shock that redirects the compressed flow along a narrow channel until the material gathers in a dense plug in the interior region of the bow shock. Then instead of calling knot T the "Mach disk," the term "refocusing shock" may be more appropriate. However, this interpretation suffers from the difficulties in extrapolating the density structures shown in the simulations to the *emission-line* structures that we observe, coupled with the incomplete treatment of magnetic fields and

non-equilibrium radiative cooling below 10^4 K in the simulations.

Presuming that knot T represents the inner shock that decelerates the jet material, the flow velocity of the jet at the working surface, V_j, can be estimated from equation (9) in Paper I using $V_{BS} = 95 \pm 20$ km s^{-1}, $V_{med} = 305 \pm 85$ km s^{-1}, and an estimated $V_{MD} \approx 30 \pm 10$ km s^{-1}. We derive a flow velocity of $V_j \sim 430 \pm 115$ km s^{-1}. Then we can balance the ram pressure at the jet and bow shocks (with eq. [11] of Paper I), using values of $V_{MD} = 30$ km s^{-1}, $V_{BS} = 95$ km s^{-1}, and $n_0 = 200$ cm^{-3}, to find that $\beta n_j \approx 2000$ cm^{-3}. For the case of a heavy jet with radiative cooling, $\beta \approx 1$ (Blondin et al. 1990), so that $n_j/n_0 = \eta \approx 10$. This value for η is similar to that derived for HH 34 in Paper I. We should qualify this result by noting that the Mach disk may not maintain a constant velocity relative to the bow shock over long time scales. Such a high value of $n_j \sim 2000$ cm^{-3} combined with the observed electron densities of less than 200 cm^{-3} in knot T also requires that the ionization fraction across the putative Mach disk be only a few percent, allowing for some compression across the shock, and may exclude shock velocities as high as 40 km s^{-1}. However, if there is a substantial magnetic field in the *jet* material entering the Mach disk, energy is consumed compressing the field rather than ionizing the incident gas, resulting in a somewhat lower peak ionization and lower excitation emergent spectrum. Additionally, if the reddening and, thus, the preshock density, have been overestimated, the value for n_j may be significantly decreased, though the density ratio, η, which depends only on the shock velocities, is unaffected by errors in the reddening correction.

5. CONCLUSIONS

We have presented the results of a detailed study of working surface dynamics at the head of the HH 111 stellar jet from observations obtained with an imaging spectrophotometer. Monochromatic images of the [S II] λ6716/λ6731 and [S II] (λ6716 + λ6731)/Hα line ratios produce maps of postshock electron densities and excitation conditions throughout the entire flow volume. We estimated a bow shock velocity of $\sim$95 km s^{-1} based on the observed bow shock shape, the absence of [O III] emission, the velocity dispersion, and the spatial distribution of the [S II] and Hα emission. We measured the Hα flux at the apex of the bow shock to estimate a preshock density of $n_0 \approx 200$ cm^{-3}, given our estimates of the bow shock velocity and reddening toward HH 111V.

A new bow shock model for HH 111V has been constructed using the geometry described in Hartigan et al. (1987) and a dense grid of planar shock models with Orion abundances reported by Osterbrock et al. (1992). The model matches the observed Hα emission-line fluxes and the [S II] λ6716/λ6731 line ratios, but only matches the [S II] fluxes well toward the leading edge of the bow shock. This lack of agreement may suggest that it is inappropriate to model the recombining emission behind the bow shock by one-dimensional planar shock models if the cooling distance is larger than the radius of curvature of the bow shock.

The models for HH 111V show that the medium ahead of the bow shock moves at a velocity of $\sim$305 km s^{-1} away from the source, possibly due to previous eruptions of the outflow. We also argue that knot T, found along the jet axis upstream from the bow shock toward the stellar source, is likely to be the Mach disk in this outflow based on its spatial location and kinematic association with the emission from the apex of the bow shock. This identification differs from the Reipurth et al. (1992). The Mach disk has a low excitation spectrum with [S II]/Hα ratios >3 and electron densities <200 cm^{-3}, indicating a very low velocity ($\sim$20–40 km s^{-1}) shock. A simple ram pressure argument shows that the jet is $\sim$10 times denser than the material ahead of the bow shock HH 111V.

Given the bow shock velocity, preshock density, and postshock electron densities measured at different points along the bow shock, we estimated a magnetic field of $B_0 \approx 30$ μG in the preshock gas of HH 111V. The ram pressure of the preshock gas exceeds the magnetic energy density by roughly three orders of magnitude, so the magnetic field is *not* strong enough to divert the flow, and the field is carried out by the jet as the flow evolves. However, the magnetic field is strong enough to inhibit the compression behind the bow shock, extending the postshock cooling region to several arcseconds.

We attribute the stratified emisson structure over the entire bow shock to a resolved cooling distance, where the Hα emission arises predominantly from collisional excitation immediately behind the shock and the [S II] emission comes from the recombination zone downstream. The presence of a magnetic field may contribute significantly toward extending the postshock cooling distance to resolvable scales.

We wish to thank the staff at CTIO for their support, especially R. Schommer who operated the Fabry-Perot during the observing run. We also thank J. Blondin (the referee), A. Raga, and B. Reipurth for their helpful comments. J. A. M. and G. C. were supported by the NSF.

REFERENCES

Allen, C. W. 1973, Astrophysical Quantities (London: Athelone)
Atherton, P. D., Taylor, K., Pike, C. D., Harmer, C. F. W., Parker, N. M., & Hook, R. N. 1982, MNRAS, 201, 661
Bland, J., & Tully, R. B. 1989, AJ, 98, 723
Blandford, R. D., & Rees, M. J. 1974, MNRAS, 169, 395
Blondin, J. M., Fryxell, B. A., & Königl, A. 1990, ApJ, 360, 370
Blondin, J. M., Königl, A., & Fryxell, B. A. 1989, ApJ, 337, L37
Cardelli, J. A., Clayton, G. C., & Mathis, J. S. 1989, ApJ, 345, 245
Cox, D. P. 1972, ApJ, 178, 143
Cox, D. P., & Raymond, J. C. 1985, ApJ, 298, 651
Gouveia Dal Pino, E. M., & Benz, W. 1993, ApJ, submitted
Hamuy, M., Walker, A. R., Suntzeff, N. B., Gigoux, P., Heathcote, S. R., & Phillips, M. M. 1992, PASP, submitted
Hartigan, P. 1989, ApJ, 339, 987
Hartigan, P., & Raymond, J. C. 1993, ApJ, in press.
Hartigan, P., Raymond, J. C., & Hartmann, L. 1987, ApJ, 316, 323 (HRH).
Hartigan, P., Raymond, J. C., & Meaburn, J. 1990, ApJ, 362, 624
Hartmann, L., Hewett, R., Stahler, S., & Mathieu, R. D. 1986, ApJ, 309, 275
Heathcote, S. R., & Reipurth, B. 1992, AJ, 104, 2193
Königl, A., & Ruden, S. P. 1992, in Protostars and Planets III, ed. E. H. Levy & M. S. Matthews (Tucson: Univ. Arizona), in press
McCall, M. L. 1984, MNRAS, 208, 253
Mendoza, C. 1983, in IAU Symp. 103, Planetary Nebulae, ed. D. R. Flower (Dordrecht: Reidel), 143
Morse, J. A., Hartigan, P., Cecil, G., Heathcote, S. R., & Raymond, J. C. 1992, ApJ, 399, 231 (Paper I).
Morse, J. A., Heathcote, S., Hartigan, P., & Cecil, G. 1993, AJ, submitted
Ohtani, H. 1980, PASJ, 32, 11
Osterbrock, D. E., Tran, H. D., & Veilleux, S. 1992, ApJ, 389, 305
Raga, A. C. 1988, ApJ, 335, 820
Raga, A. C., & Binette, L. 1991, Rev. Mexicana Astron. Af., 22, 265
Raga, A. C., & Mateo, M. 1988, AJ, 95, 543

Raymond, J. C. 1979, ApJS, 39, 1
Raymond, J. C., Hartigan, P., & Hartmann, L. 1988, ApJ, 326, 323
Reipurth, B. 1989a, Nature, 340, 42
———. 1989b, in ESO Workshop on Low Mass Star Formation and Pre-Main Sequence Objects, ed. B. Reipurth (Garching: ESO), 247
Reipurth, B., & Heathcote, S. R. 1991, A&A, 246, 511
———. 1992, A&A, 257, 693
Reipurth, B., & Olberg, M. 1991, A&A, 246, 535
Reipurth, B., Raga, A. C., & Heathcote, S. 1992, ApJ, 392, 145 (RRH)
Stone, J. A., Mihalas, D., & Norman, M. L. 1992, ApJS, 80, 819
Stone, J. A., & Norman, M. L. 1993, ApJL, submitted
Vallée, J. P. 1989, A&A, 224, 191
Vogel, S. N., & Kuhi, L. V. 1981, ApJ, 245, 960